DEUTSCHES ELEKTRONEN – SYNCHROTRON

DESY SR 91-02
December 1991

A Scanning Soft X-Ray Microscope with an Ellipsoidal Focussing Mirror

J. Voß, H. Dadras, C. Kunz, A. Moewes,
G. Roy, H. Sievers, I. Storjohann, H. Wongel
II. Institut für Experimentalphysik, Universität Hamburg

ISSN 0723-7979

NOTKESTRASSE 85 · D-2000 HAMBURG 52

To be sure that your preprints are promptly included in the HIGH ENERGY PHYSICS INDEX, send them to the following (if possible by air mail):

DESY Bibliothek Notkestraße 85 W-2000 Hamburg 52 Germany	DESY-IfH Bibliothek Platanenallee 6 O-1615 Zeuthen Germany

DESY SR 91-02
December 1991

A SCANNING SOFT X-RAY MICROSCOPE WITH AN ELLIPSOIDAL FOCUSSING MIRROR

J. Voß, H. Dadras, C. Kunz, A. Moewes, G. Roy,

H. Sievers, I. Storjohann and H. Wongel

Universität Hamburg
II. Institut für Experimentalphysik,
Luruper Chaussee 149,
D-2000 Hamburg 50, FRG

We have developed and brought into operation a new type of scanning soft X-ray microscope which can operate at any photon energy from 20 to 1300 eV. This microscope demagnifies a diaphragm by means of an annular section of an ellipsoidal mirror to a smallest spot size of presently about 0.4 µm (FWHM), certainly containing only a small fraction of the total intensity. The sample is scanned across this spot. Between mirror and focus a free space for detectors of 30 mm is available and particles emitted from a surface at more than 30° to the normal can be extracted into a mass or energy analyser. Transmission, photoemission, luminescence, photostimulated desorption, reflectivity and other signals may serve for imaging. In addition, a static analysis of very small samples or spots on a sample will become feasible.

to be published in: Journal of X-Ray Science and Technology

ISSN 0723-7979

1. Introduction

Nowadays there exist a host of different types of microscopies and each of them has its own merits. While the general goal of all microscopies is to achieve high resolution, they also display objects with different types of contrast. There lies the main objective of developing such a manifold of different microscopic methods.

The idea to generate images in the light of x-rays came up right after their discovery; it was, however, hampered by the fact that there exist no lenses comparable to those in ordinary light optics. In spite of this fact many efforts have been made during the years to overcome this problem (1-4). Practically all attempts are restricted to the soft x-ray regime, namely photon energies below about 1000 eV. Imaging can be achieved by Fresnel zone plates and by different types of mirrors. Further, scanning microscopy can sometimes be performed with much simpler optics, in the simplest case by putting the sample behind a pin-hole. When a microfocus of soft x-rays is generated not only transmission but also secondary processes like photoelectric emission, ion desorption, luminescence etc. may serve to obtain images. This type of microscopy bears the advantage that the observed contrast is often readily interpreted in terms of fundamental physical processes. In addition, the imaging of photoelectrons which are emitted from a wide range of the sample should be mentioned.

Soft x-ray microscopy was markedly revived with the advent of synchrotron radiation (5-8). These new efforts are well documented

in a series of conference proceedings (2-4). By far the most advanced project is that of the Göttingen group (9, 2-4). This group has developed both imaging and scanning microscopy with zone plates holographically produced as optical elements. They apply this microscopy exclusively for the investigation of biological objects in the so-called water window between 300 and 500 eV photon energy. Other well advanced zone plate microscopes, all operating in the scanning transmission mode, are those of Kirz et al.(10) and of Burge et al. (11).

Ade et al. (12) recently succeeded in operating a scanning photoemission microscope using a zone plate incorporated in a cylindrical mirror electron analyser. In our laboratory Haelbich et al. (13-15) have developed a scanning microscope based on a Schwarzschild objective coated with reflection enhancing multilayers. This idea was recently revived in the MAXIMUM project (16).

Photoemission microscopes with electron imaging are presently developed by Tonner (17), Harp et al. (18) and Pianetta et al. (19). Also several groups are developing such microscopes with classical light sources in the far ultraviolett (20-23) where differences in work function at surfaces create pronounced contrast.

Aoki et al. (24) and Franks et al. (25) have obtained images using grazing incidence reflection from two consecutive surfaces in a Wolter type (26, 27) arrangement.

Our project, (first reported at the London Conference on X-Ray Microscopy (4)) is based on the idea that a scanning microscope does not need to image a whole field but only needs to concentrate light in a small spot. This can be achieved by a single reflecting surface at grazing incidence. The appropriate surface is a section of a rotational ellipsoid (see Fig. 1). The advantages of a grazing incidence reflecting optics lie in the fact that it can operate at any photon energy below the cut off energy of specular reflection in one and the same alignment. This is especially suited for use with synchrotron radiation and is ideally fitted to a beam line we have been operating at HASYLAB for several years. The FLIPPER monochromator (28) delivers monochromatic radiaton from an undulator which can be tuned from 36 to above 1000 eV. Below 36 eV synchrotron light is available in the wiggler mode down to 20 eV. It is therefore also conceivable to operate the microscope with a band of photons comprising the full width of an undulator peak thereby gaining several orders of magnitude in intensity. The general considerations to be made in comparing different types of optics and microscopes are published in more detail elsewhere (29, 30).

There is another important advantage of this type of microscope. In the arrangement, which we chose, an unobstructed region of 30 mm is available in front of the sample for inserting detectors for electrons, for luminescence radiation, and for secondary particles. Particles leaving the sample under an angle of less than 150° to the direction of the incoming light can bypass the mirror on one side and can be guided into bulky detectors. Some other

properties of this microscope will become obvious after the detailed discussion below.

We want to mention here a few possible applications of such a microscope. Surface reactions, like e.g. oxidation, which are presently studied on homogeneous samples could be carried out on artificially structured samples as e.g. chips, on polycristalline samples where oxidation can start on specific surfaces or at grain boundaries, on stepped samples, where the oxidation can take place on terrace surfaces or at steps. Similarily reactants could be identified on other samples, like e.g. on inhomogeneous catalysts. Difference pictures and pictures where photoelectrons of specific characteristic energies are filtered could show the distribution of one kind of atom or molecule and even select it in a well defined binding state. Insulating materials could be investigated (in fluorescence or with the technique of ion desorption) since they are usually inaccessible to methods which require electron bombardment. The same holds for organic samples which are destroyed very fast by electron beams while photon irradiation is much gentler in general. New materials which are sintered the way the high T_c superconductors are prepared could be scanned for small single crystals which would be homogeneous enough to display the properties of the pure material. The sensitivity of the method as a microprobe in environmental research for certain elements located at the surface of dust particles needs further exploration, but looks very promising. Dangerous substances which one would not like to put into a sample chamber in macroscopic quantities could be investigated on microsamples specially prepared. In Chapter 2 we shall describe the general arrangement of the microscope and its theoretical limita-

tions. In Chapter 3 details of the construction are given while Chapter 4 is devoted to alignment, first tests and first images.

2. Optics

2.1 Layout of the Optics

Fig. 1 shows the general layout of our microscope. It can easily be shown that a rotationally symmetric, ring shaped mirror has two fundamental problems. The most serious one is that such a mirror cannot image an extended area point by point in grazing incidence, the field is reduced to a single point on the axis. Wolter (26, 27) has therefore designed arrangements involving two consecutive reflections which avoid this problem. A sufficiently small sector of an elliptical ring mirror would allow imaging with a certain degree of accuracy. Because of symmetry and diffraction considerations, however, we want to use the full ring. This problem is overcome in our arrangement by centering the circular object diaphragm at one focal point of the ellipsoid. In this case, all rays emerging from this diaphragm are collected in the image plane in a demagnified circle.

The second problem arises from the fact that the demagnification is not the same for rays reflected at different points along the axis. This limits the usable length of such mirrors. First we analyse the set-up in terms of geometrical optics. The parameters of the microscope are chosen in such a way that the emission of the

FLIPPER monochromator (28) is matched to the acceptance of the microscope as well as possible. Further the 2° grazing angle of reflection on the ellipsoid allows us to operate the microscope safely over the full energy range of the monochromator which extends from 20 to 1300 eV. In detail, the following considerations were made:

1. The overall length should not be not more than about 1 m in view of the available space and in order to easily place the instrument on a single vibrationally isolated granite block.

2. The demagnification 1 : 30 results in a large enough working distance of 35 mm between ellipsoid and sample. This demagnification would allow us to obtain a 0.1 µm focus with a 3 µm diameter entrance diaphragm on the assumption of purely geometrical imaging.

3. The 2° grazing angle on a gold coated mirror allows specular reflection of radiation up to about 2000 eV with reasonable efficiency with requirements on surface smoothness considerably relaxed. The Beckmann factor (31), which describes the reduction of specular reflectivity due to scattering losses, yields an 1/e-intensity drop at 1400 eV photon energy with a mean square roughness of 2 nm. At 700 eV photon energy the specular reflectance needs to be corrected by a factor of 0.78 only.

4. The entrance diaphragm of our microscope replaces the exit slit of the FLIPPER monochromator. It is aligned there by means of a preadjusted telescope. The focusing paraboloid of the monochromator serves as a condensor and produces images of the source in the storage ring which are about 300 µm wide horizontally and

vertically dispersed. They are about 50 μm high for an individual wavelength. The diaphragm transmits a certain fraction of this image. A condensor mirror with higher shape accuracy could reduce the horizontal width of the image and thereby collect more light into the diaphragm.

5. The annular shaped aperture in front of the ellipsoidal mirror accepts a hollow cone of radiation 5 mrad in diameter. The monochromator offers radiation in an angular range 30 mrad horizontally and 7 mrad vertically down to 10 mrad horizontally and 5 mrad vertically depending on the energy region. Because of the undulator emission pattern (6) convoluted with the angular spread of the electron beam in the DORIS storage ring at the position of the undulator W1 (28), intensity is not distributed uniformly in this aperture. There is higher intensity in a central region matching approximately the acceptance cone of the ellipsoid.

6. The length of the mirror of 6 mm was chosen in order to facilitate manufacturing. If technically feasible, it could be enlarged to about 15 mm.

2.2 Intensity

A rough estimate of the intensity to be expected in the focus can be carried out. The basis is given by the measured intensity behind the 200 μm wide exit slit of the FLIPPER monochromator as displayed in Fig. 2. The ratio of the area of a 15 μm diaphragm to the 300 μm x 200 μm wide beam at the exit slit gives a loss factor of $3 * 10^{-3}$, the angular acceptance of the annular diaphragm in

front of the ellipsoidal mirror divided by the angular spread of the monochromatic beam gives a loss factor of $1.5 * 10^{-2}$, as a general reflectivity we take 0.8. This gives an overall loss factor compared to the output curves of the monochromator in Fig. 2 of $3.6 * 10^{-5}$. This estimate should be considered as a lower limit since it is based on a uniform intensity distribution both in the focus of the beam at the exit slit and in the angular spread of radiation. The angular distribution of radiation from an undulator, however, is not uniform (see point 5 in Section 2.1).

The result of our measurements which will be described below is also indicated in Fig. 2.

2.3 Imaging Quality

In order to analyse imaging in our microscope in more detail we introduce the following functions:

O (x,y), the object function characterizes the contrast of the object,

I (x,y), the image function gives the contrast distribution of the image,

P (x,y), the point spread function (PSF) is the intensity distribution of the probe.

The PSF is determined by the parameters of the optical system as there are size and location of the source, spatial and temporal coherence, aperture function, errors of imaging, wavelength and diffraction.

These three functions obey the following relation

$$I(x,y) = O(x,y) * P(x,y), \qquad [1]$$

where * denotes convolution. The respective Fourier transforms are then combined by multiplication according to

$$I(k_x,k_y) = O(k_x,k_y) \cdot P(k_x,k_y) \qquad [2]$$

where k_x,k_y are spatial frequencies (multiplied by 2π). $P(k_x,k_y)$ is called the optical transfer function (OTF). Since the OTF is a complex function it can be described by

$$P(k_x,k_y) = MTF(k_x,k_y) \exp[i\, PTF(k_x, k_y)] \qquad [3]$$

where $MTF(k_x,k_y)$ is the modulation transfer function which describes the attenuation of the amplitude of a periodic structure from the object to its image. In the case of rotational symmetry of the PSF the PTF (phase transfer function) is zero and no phase shift will occur.

For periodic structures contrast C is defined by maximum and minimum intensities I_{min} and I_{max} in the image function as

$$C = \frac{I_{max} - I_{min}}{I_{max} + I_{min}} \qquad [4]$$

A resonable and widely accepted criterion for defining the spatial resolution Δr of an optical system is to take the value where $P(2\pi/\Delta r,0)$ becomes zero, i.e. where the contrast C vanishes. For a one-dimensional object function O(x) contrast is given by

$$C = \frac{MTF(k_x)}{MFT(0)} \qquad [5]$$

We have analysed the MTF for our arrangement taking into account the slope errors of the mirror and diffraction.

2.3.1 Alignment

Ray tracing calculations show the behavior of the focus of the mirror if the diaphragm is not properly centered on the axis and if the sample is not located in the focal plane. It turns out that the result of this ray tracing can be worked out analytically and leads to a mathematical expression which allows calculating the image (I) of a point source (S) (see Fig. 3) displaced from the axis. In general, it is a line focus identified as Pascal's helix. Its analytical representation is given by:

$$OP = \begin{pmatrix} (1+\eta+\xi')r\cos 2\beta - (\eta+\xi)R\cos\beta \\ (1+\eta+\xi')r\sin 2\beta - (\eta+\xi)R\sin\beta \\ c+\Delta I_{ax} \end{pmatrix} \begin{pmatrix} \cos\phi & -\sin\phi & 0 \\ \sin\phi & \cos\phi & 0 \\ 0 & 0 & 1 \end{pmatrix}, \qquad [6]$$

The matrix on the right side rotates Pascal's helix given by the first term on the right hand side depending on the azimuth ϕ of the displacement (see Fig. 3).

The parameters η, r, c, ξ, ξ', $\beta = \theta - \phi$ and R are given by:

$$\eta = \Delta I_{ax}/f_I \qquad \xi = \Delta S_{ax} f_I/f_o$$

$$r = \Delta S_{lat}\, f_I/f_o \qquad R = [a^2-(c-f_I)^2]^{\frac{1}{2}} \qquad [7]$$

$$c = [a^2 - b^2]^{\frac{1}{2}} \qquad \xi' = \Delta S_{ax}/f_o$$

a and b are the large and the small half axis of the ellipsoid ϕ, Θ. ΔI_{ax}, ΔS_{ax}, ΔS_{lat}, f_o and f_I can be taken from Fig. 3.

Fig. 4 gives the result of typical misalignments by ray-tracing calculations, calculated analytically from Eq. [6]. In operating the microscope such patterns serve to determine the misalignment and to correct the parameters in a controlled way in order to obtain a PSF as small as possible.

2.3.2 Surface Errors of the Mirror

The influence of the gradient errors of the reflecting surface have been calculated in a simple theoretical approach assuming the meridional and sagittal gradient mean square errors Θ_m and Θ_s to be independent and of Gaussian distribution. The resulting PSF is presented in Fig. 5a, the corresponding contrast given by the normalized MTF is presented in Fig. 5b. In the case of vanishing of both Θ_m and Θ_s the PSF is the Delta function with a contrast of 1. If only Θ_m or Θ_s is equal to zero, the PSF will contain an integrable singularity while the contrast is given by the function marked $\eta = 0$.

The best mirror until now (Θ_m= 2.2" rms; Θ_s= 20" rms) creates a spot of 0.4 µm (FWHM) in agreement with this calculation.

The reduction of the specular reflectivity R_{spec} by the Beckmann factor B (31) due to roughness (σ= 2 nm) decreases the contrast in a similar way, where

$$B = \exp[-(4\pi\sigma\sin\theta/\lambda_{ph})^2], \qquad [8]$$

with Θ the grazing angle of incidence. It has been shown that applying this factor in this wavelength range gives reasonable results (31). It varies from 1 at 100 eV to 0.46 at 1300 eV, λ_{ph} is the wavelength of the photons.

2.3.3 Diffraction

Finally, the diffraction limit of this microscope needs to be analysed. It turns out that a strict mathematical analysis of this problem is quite intricate. The basis of such an analysis is the Helmholtz-Kirchoff integral method. Two complications arise, one of which is due to the fact that a mirror is involved which in this special case unlike a lens cannot just be considered as an element which transforms the diffraction image from infinity into the image plane. The other complication is the high sensivity of the diffraction pattern of an annular aperture to the degree of coherence of the illumination. Therefore, a series of calculations and considerations had to be undergone in order to obtain a prediction of the behaviour under realistic circumstances. Here we give only a simplified analysis which is sufficiently accurate for a general understanding of the behaviour and the limitations of the microscope.

To estimate the essential features of the diffraction pattern of the ellipsoidal mirror we use the Debye-Plane-Wave-Approximation which leads to the Airy formula for Fraunhofer diffraction in the geometrical focal plane. The central obstruction causes a modification of

the well-known intensity distribution of the diffraction pattern of a circular aperture.

Assuming coherent illumination of an annular aperture bounded by two concentric circles of radii a and ea (e<1) the intensity is given by

$$I \quad [2J_1(x)/x-2eJ_1(ex)/x]^2 \qquad [9]$$

where $J_1(x)$ is the Bessel Function of the first order. Figure 6a shows a model calculation for the value of e which applies to our specific mirror.

By increasing e from 0 to 1 the radius r of the first dark ring decreases by a factor of 1.6 and gives

$$r = 0.38\ \lambda_{ph}L/a, \qquad [10]$$

where λ_{ph} is the photon wavelength and L the distance between the aperture and the focal plane. This improvement in the resolving power, on the other hand, is accompanied by a deterioration in the contrast because the higher orders become more pronounced relative to the central maximum. The relative increase of the higher orders (see Fig. 6b) lowers the fraction of the 0th order in the total intensity from 84% for the circular aperture to 7.2% for the annular aperture as used in the microscope. In the limiting case of e = 1 it yields an intensity distribution, proportional to the square of the zeroth order Bessel function

$$I \quad [J_0(x)]^2 \qquad [11]$$

resulting in contrast zero. By inserting the geometrical parameters of the microscope we obtain a diffraction pattern as shown in Fig. 6a and integrated intensities as shown in Fig. 6b. The radius of the first dark ring of the diffraction fine structure, which can be employed as a measure of the resolution of our microscope has a value of

$$r = 6\lambda_{ph}. \qquad [12]$$

The radius of the first dark ring of the enveloping structure, determined by the length of the mirror, is larger by a factor of nearly 30 to

$$R = 178\lambda_{ph}. \qquad [13]$$

The result of the calculation of the MTF is presented as the continuous line in Fig. 6c. Its zero gives a best resolution of λ_x = 6.7 λ_{ph} and a local maximum at $\lambda_x = 7.7\lambda_{ph}$ with a contrast of 0.06.

It is important to have an estimate also for the resolution in the case of non-coherent illumination. As a coarse estimate a "restricted" coherence was the basis of a detailed analysis. It means coherent illumination only for small segments of the annular aperture treated as rectangular slits with a constant intensity distribution in radial direction and a Gaussian distribution along the circumference. The resulting diffraction pattern integrated over the whole circumference leads to an irradiance distribution given by the envelope of the strongly oscillating curve in Fig. 6a. Also in

this case, the MFT was calculated and is presented as the dotted line in Fig. 6c. It is evident that the difference between this MTF and the MTF in the coherent case is rather small over a wide range. An appreciable gain of a resolution by a factor of 3 is only given at the local maximum at $\lambda_x = 7.7\lambda_{ph}$.

3. Technical realization of the instrument

3.1. Layout

Figure 7 shows the schematic arrangement of the components of the microscope on a granite block. It was neccessary to consider vibrational isolation as an important factor from the very beginning. All components should be contained in a UHV system in order not to spoil the vacuum of the adjacent monochromator and also in order to be able to do in situ surface investigations on clean samples and on samples exposed to adsorbates under controlled conditions. A further requirement was long-time stability of the alignment under the conditions of the HASYLAB-laboratory where no air conditioning is provided. If necessary, a thermal isolation or temperature stabilisation could be built around the instrument. This, however, should be avoided out of practical considerations, if possible. Therefore, all sensitive components were manufactured out of INVAR 36 , an alloy which has a ten times lower expansion coefficient than ordinary steel. In spite of its mass the whole instrument needs to be aligned very accurately with respect to the focus and the direction of the beam provided by the FLIPPER monochromator. Alignment of the ellipsoidal mirror and scanning

of the sample should be driven and monitored from outside the vacuum and coupled into the system with bellows. This decision was made after several attempts to find solutions with piezo and other actuators inside the vacuum. It turned out that monitoring the actual motions under UHV-conditions proved to be either impossible or forbiddingly expensive.

The granite block weighing 700 kg rests on four 10 cm thick rubber supports in a heavy steel frame. The system has a characteristic frequency of 5 Hz. The steel frame is supported by three legs one of them right below the entrance diaphragm. On activation of compressed air valves the legs are lifted by about 40 µm and can slide on a smooth floor. Their motion is controlled by micrometer screws. Additional screw-jacks allow to adjust the legs individually. Thus there are all the degrees of freedom neccessary to align the entrance diaphragm relative to the beam and to direct it to an optimal illumination of the annular aperture in front of the ellipsoidal mirror. When the original exit slit of the monochromator is removed a telescope viewing over a split 45 deg mirror fixes the position with a reticule. This is neccessary since the vertical position determines the focusing and the alignment of the monochromator. The whole instrument is mounted on the same separately founded platform which also supports the FLIPPER monochromator. The vacuum system is supported on the steel frame but it is separated completely from the granite block which is the support of the entrance diaphragm, the mirror and the sample. The two turbomolecular vacuum pumps are vibrationally isolated by bellows and could be mounted on separate supports on a different platform. Up to now, this did not prove to be neccessary.

3.2. The Mirror

The small inner diameter of the ellipsoid does not allow direct diamond turning and polishing. The Zeiss company therefore decided to apply a replication technique. A mandrel with the shape of the ellipsoid is fabricated by single point diamond turning and computer controlled polishing. The process is monitored by frequent measurements. Then the mandrel is coated with gold and replicated in expoxy which is supported by an aluminium ring. The inner surface of this ring is preshaped also to an ellipsoid as good as possible in order to keep the epoxy layer thin and uniform. After hardening of the epoxy the gold surface is separated from the mandrel.

Our goal for the first phase of the project was to obtain an accuracy which should allow a focal width of 0.4 μm. The microroughness should not result in any large reduction of the specular reflectivity up to 1300 eV. Therefore, the following tolerances were given:

- roundness error less than 10 nm rms,
- surface gradient less than 0.5" rms,
- microroughness less than 2 nm rms.

For the best mirrors as delivered up to date the values of the first two specifications are larger by almost one order of magnitude. Probably, it is necessary to find better techniques in order to achieve gradual improvements towards the original goal.

3.3. Alignment

The entrance diaphragm has to be brought to a fixed position roughly in the center of the vacuum tube. Then the axis of the elliptical focussing mirror needs to be aligned in such a way that it hits the center of the entrance diaphragm. In order to be prepared also for future improvements in mirror fabrication, we aimed at a reproducibility of 1 μm which means angular alignment to within 0.2 sec of arc. The mirror is mounted on a support which can be tilted coarsely by counteracting screws, fine alignment is made by piezo elements. The two angular motions are monitored by means of an external autocollimation system which was built for that purpose. Its accuracy is better than ± 1 μrad, over a range of 2mrad in both directions. The sample is fixed to the same support as the mirror so that the axis of the mirror hits the sample always at the same point during alignment. This is the position where the focal spot will finally be centered if the alignment procedure is completed. The holder of the two sets of entrance diaphragms acutally consists of two independently adjustable elements 1 mm apart in the direction of the beam (z-direction). They are mounted in a 35 mm UHV double cross. Flexible bellows allow alignment in the x-direction (horizontally) and the y-direction (vertically). The first holder contains 1 mm, 100 μm, and 50 μm diaphragms, the second holder contains 200, 50, 35, 25, 15, 8, and 4 μm diaphragms. Usually, the first holder remains fixed with the 100 μm diaphragm in place in order to fix the position of the beam while the finer diaphragms are exchanged.

3.4 The Scan Mechanism

Scanning of the sample in the image plane as well as focusing along the optical axis is done by three linear actuators. These elements are mounted directly on the table which serves to align the mirror outside of the vacuum system. The motion is coupled through bellows into the ultra high vacuum chamber, where three rods are coupled to form an orthogonal tripod (Fig. 7).

Each of the three elements (Fig. 8) consists of a lever arm system with flexible joints. The levers transfer the motion of a micrometer screw at a gear ratio 1 to 1 and that of a piezo translator at a gear ratio 1 to 3. In order to guarantee maximum mechanical and thermal stability, these elements were manufactured by spark erosion from massive blocks of INVAR 36.

The measurement of the actual position of the motion of the sample in a $(3mm)^3$ volume is performed with a scale which moves parallelly with respect to a fixed measuring system (Heidenhain). A feedback system allows a reproducibility of 40 nm. The accessible image volume has a size of $(150\ \mu m)^3$ if the piezo elements are used alone and $(3\ mm)^3$ if manual activation is used by means of the micrometer screws.

3.5 Manipulation and Detection

Before the microscope can be operated, a number of alignments have to take place. These need several different measuring systems to characterize the alignment.

Optical pre-alignment of the entrance aperture relative to the focus of the FLIPPER monochromator is achieved by means of a telescope which views the visible part of synchrotron radiation at the position of the entrance aperture. In order to optimize the illumination of this diaphragm, a gold coated, calibrated cathode which measures the photoemission current serves as a detector. It can be inserted between the diaphragm and the ellipsoidal mirror.

The degree to which the ring aperture of the mirror is uniformly illuminated is controlled among other means by two GaAsP-Schottky diodes, one in front of the mirror mounted directly on the central beam stop which can also be used as a reference during measurements and one behind the mirror. For measuring transmission of samples there are two further detectors available, one of them another GaAsP-Schottky diode, the other one a channeltron. An additional channeltron between the mirror and the sample serves to measure total photoemission yield.

A 150° spherical electron analyser has been installed to combine microscopy and photoelectron spectroscopy. The analyser shown in Fig. 9 has a mean radius of 50 mm and an energy resolution of $E/\Delta E = 75$. Because of the long working distance between the mirror and the sample a specially designed four element electron lens imaging the electrons emitted from the sample onto the entrance slit of the analyser could be added.

The coarse alignment of the ellipsoid is done by using the visible part of the discharge lamp or the synchrotron radiation in 0th order

of the monochromator. With a moderately magnifying telescope the sample surface can be examined over a deflecting plane mirror. The pattern in the image plane serves to identify coarse misalignments. The limit of this procedure lies at a focal spot size of about 5 μm. Since yet there exists no transfer mechanism in order to change samples and bring them from the outside into the vacuum system, we had to find a solution to mount different samples in the recipient. In order to be able to exchange samples, a small wheel with 20 positions was mounted at the actuator. Due to friction, this wheel would stay fixed with one sample in place at a time. Changing of samples is achieved by coupling a wobble stick to the wheel and pushing it from one to the next position.

4. First Results

4.1 Criteria for Alignment

As explained in Chapter 2.3.1, misalignments of the mirror yield intensity distributions without rotational symmetry outside the focal plane. Our experience shows that a criterion which only looks for maximum intensity at a spot in the intensity distribution leads with almost certainty to a complete misalignment. In this case, a Pascal's helix results with an inner ring contracted to a point. Based on this behaviour integral alignment methods as e.g. the knife edge test are very difficult to apply with a positive result.

In order to be able to obtain an optimum alignment of the microscope, it is necessary to have information on the complete

intensity distribution in the actual image plane. For that purpose a pinhole is used to scan the image plane. The observed images are a two-dimensional convolution of the pinhole transmission function with the actual intensity distribution. An additional difficulty is caused by a non-uniform illumination of the mirror aperture. Due to imperfections of the optical components in the FLIPPER monochromator, which serves as a condensor, the intensity distribution at the entrance aperture of the ellipsoidal mirror is concentrated in horizontal lines. Therefore, the analysis of the measured focal patterns proves to be much more difficult than theoretically predicted.

4.2 Resolution

In Fig. 10 a line scan through the focus is shown with visible laser light at 2 eV photon energy. The radius of the first dark ring due to diffraction is 3.6 μm. The diffraction pattern could be resolved up to the 19th order and agrees well with the calculations.

With radiation at 21.2 eV from a He discharge source, the focus is limited by diffraction to a size of 0.4 μm. The experimental curve displayed in Fig. 11 almost reaches this limit with a halfwidth smaller than 0.35 μm. The fine structure of the diffraction pattern cannot be resolved spatially any longer. Due to the small intensity the secondary diffraction structure is not visible either. Intensity in in the first order maximum is theoretically already reduced to 10^{-4} of the central maximum.

In the logarithmic display (Fig. 12) the errors of the mirror can be

detected. The sharp central peak of the focus is superimposed on a broad halo with a radius of 20 μm. The background measured over the whole range is a consequence of the inefficient suppression of light reflected several times in the UHV chamber.

In Fig. 13 a focal scan at 1100 eV is presented. In this case the central spot is surrounded by scattered light due to roughness of the ellipsoidal mirror. Although we are unable for the moment to do a quantitative evaluation of the actual roughness σ of the mirror there are indications from photon energy dependent measurements that it is in the order of 2 nm or somewhat larger.

In Fig. 14 the symmetry of rotation of the light spot is demonstrated in a two dimensional scan in the focal plane. The halfwidth amounts to approximately 0.4 μm.

4.3 Test Objects

Images of test objects as shown in Fig. 15 and Fig. 16 a,b were measured at different photon energies between 21eV and 1100eV both in transmission and total photoelectric yield. Fig. 17 b shows a 3.7 x 4.0 μm^2 wide area of a zone plate. The total yield at a photon energy of 700 eV serves as the signal to give the image. It shows resolved spatial structures of a size of about 0.9 μm, however with

a poor contrast of less than 5%. The continuously varying grating constant of a zone plate permits a direct measurement of the MTF of the optical system. The result of an analysis of a long range

transmission linescan is given in Fig. 17. The contrast is presented as a function of the spatial frequency and decreases from 12% to 2% in the range from 0.1 μm^{-1} to 0.8 μm^{-1}.

4.4. Photoelectron Spectroscopy

For the first tests with the electron analyser several artificial structures have been investigated. In Fig. 18 the energy distribution curve at a photon energy of 330 eV of a gold spot evaporated on silicon is presented. The gold spot had a diameter of 10 μm, the focus had 3.5 μm diameter FWHM using an entrance aperture of 100 μm. In addition, the Au 4f lines could be resolved easily. The spectrum shows contributions of a contamination with carbon.
Fig. 19 shows an energy distribution curve at 120 eV taken on a copper mesh. The Cu 3d signal then serves as the signal of a linescan over 35 μm (Fig. 20). It is inverse to the structure of the accompanying transmission scan in Fig. 21. The poor contrast belongs to the imperfections of the mirror which, in this case, result in a spreading of the intensity over a region of about 20 μm in diameter.

4.5 Conclusion

The most important problem of our microscope is still the manufacturing of a high quality mirror. While all the other difficulties as alignment, scanning, stability etc. could be overcome, the technical difficulties of producing an ellipsoidal surface of the required accuracy were initially underestimated. Nevertheless, the microscope in its present status can already be

employed as a promising instrument with the perspective of future developments which will increase its capabilities steadily. This microscope will profit especially from the advent of third generation synchrotron radiation sources.

Acknowledgments

This project is supported by the German Federal Minister of Research and Technology (BMFT) under contract no. 05 405 AXB, TV4. Thanks go to the workshops of DESY and the II. Institut of Experimental physics for their careful manufacturing of delicate components. We also want to acknowledge the fruitful collaboration with Drs. Becker, Beckstette and Heynacher from Zeiss.

REFERENCES

1 V.E. Cosslett and W.C. Nixon, "X-ray Microscopy", Cambridge University Press, Cambridge, 1960

2 G. Schmahl, D. Rudolph, Eds., Proceedings of the International Symposium, "X-Ray Microscopy", (Göttingen, 14-16 Sept. 1983) Springer Series in Optical Sciences 43, Springer, Berlin, Heidelberg, 1984

3 D. Sayre, M. Howells, J. Kirz, H. Rarback, Eds., Proceedings of the International Symposium, "X-Ray Microscopy II", Brookhaven 31. Aug. - 4 Sept. 1987, Springer Series in Optical Sciences 56, Springer Berlin, Heidelberg, 1988)

4 A. Michette et al. Eds., Proceedings of the International Symposium, "X-ray Microscopy", London, 3. - 7. Sept. 1990, Springer Series in optical Sciences, to be published

5 C. Kunz, Ed., "Synchrotron Radiation - Techniques and Applications", Springer Berlin, Heidelberg, New York, 1979, Topics in Current Physics, Vol. 10

6 E.E. Koch, Ed., "Handbook on Synchrotron Radiation", North Holland, Amsterdam, New York, Oxford, 1983, Vol. 1a, 1b, 2

7 M. Ando, T. Miyahara Eds., "Proceedings of the 3rd Int. Conf. on Synchrotron Radiation Instrumentation", SRI 88 Tsukuba, 29. Aug.-2. Sept. 1988, Rev. Sci Instrum 60, 1373, 1989

8 R.C.C. Perera and A.C. Thompson Eds., "Proceedings of the Sixth National Conference on Synchrotron Radiation Instrumentation" Berkely 7.-10. Aug. 1981, Nucl. Instr. Meth. Phys. Res. A291, 1990

9 G. Schmahl, D. Rudolph, P. Guttmann, in Ref. 3, p. 228

10 J. Kirz, M. Ade, E. Anderson, D. Attwood, C. Buckley, S. Hellmann, M. Howells, C. Jacobsen, D. Kern, S. Lindaas, I. McNulty, M. Oversluizen, H. Rarback, M. Rivers, S. Rothman, D. Sayre, D. Shu, Physica Scripta T31, 12 (1990)

11 G.R. Morrison, M.T. Browne, C.J. Buckley, R.E. Burge, R.C. Cave, P. Charalambons, P.J. Duke, A.R. Hare, C.P.B. Hills, J.M. Kenney, A.G. Michette, K. Ogawa, A.M. Rogoyski, T. Taguchi in Ref. 3, p. 201

12 H. Ade, J. Kirz, S.L. Hulbert, E.D. Johnson, E. Anderson, D. Kern, Appl. Phys. Lett. 56, 1841 (1990)

13 R.P. Haelbich, W. Staehr, C. Kunz, in "Ultrasoft X-Ray Microscopy, Its Application to Biological and Physical Sciences" (D.F. Parsons, Ed.), New York 13-15 June 1979, Annals of the New York Academy of Sciences, Vol. 342 (1980)

14 R.-P. Haelbich, in "Scanned Image Microscopy" (A. Ash, Ed.) p. 413, Academic Press, London 1980

15 R.-P. Haelbich, Thesis, Univ. Hamburg 1980, Int. Rep. DESY F41 HASYLAB 80/03 (1980)

16 F. Cerrina, G. Margaritondo, I.H. Underwood, H. Hettrick, M.A.Green, L.J. Brillson, A. Franciosi, H. Höchst, P.M. Deluca Jr. and M.N. Gould, Nucl. Instr. and Meth. A 266, 303 (1988)

17 B.P. Tonner, Nucl. Instr. and Meth. A 291, 60 (1990)

18 G.R. Harp, Z.-L. Man, B.P. Tonner; Physica Scripta T31, 23 (1990)

19 P. Pianetta, I. Lindau, P.L. King, M. Keenlyside, G. Knapp, R. Browning, Rev. Sci. Instrum. 60, 1686 (1989)

20 H. H. Rotermund, S. Jakubith, S. Kubala, A. von Oertzen and G. Ertl, J. El. Spectr. and Rel. Phen. 52, 811 (1990)

21 M.E. Kordesch, W. Engel, E. Zeitter and A.M. Bradshaw, J. Phys. B. (in press)

22 H. Bethge, T. Krajewski, O. Lichtenberger, Ultramicroscopy 17, 21 (1985)

23 W. Telieps, E. Bauer, Ultramicroscopy 17, 57 (1985)

24 S. Aoki, in Ref. 3, p. 102

25 A. Franks, B. Gale, in Ref. 2, p. 129

26 M. Wolter, Ann. Phys. 10, 94 (1952)

27 M. Wolter, Ann. Phys. 10, 286 (1952)

28 F. Senf, K. Berens v. Rautenfeldt, S. Cramm, J. Lamp, J. Schmidt-May, J. Voß, C. Kunz, V. Saile, Nucl. Instrum. Meth. A246, 314 (1986)

29 C. Kunz, Proc. Int. School of Physics "Enrico Fermi" Course CVIII, North Holland, Amsterdam, Oxford, New York, Tokyo, 1990 p. 93

30 C. Kunz, in "X-Ray and Inner Shell Processes" (T.A. Carlson, M.O. Krause, S.T. Manson, Eds.), AIP Conference Proc. 215, AIP, New York, 1990, p. 208

31 H.G. Birken, C. Kunz, R. Wolf, Physica Scripta 41, 385 (1989)

FIGURE CAPTIONS

Fig. 1 Principle and parameters of the microscope (not true to scale), $h\nu$ marks the direction of incoming synchrotron radiation

Fig. 2 Measured photon flux at the 200 μm wide monochromator exit slit (line) and with a 15μm diaphragm replacing the exit slit after the reflection by the ellipsoidal mirror(*) (left ordinate: monochromator intensity, right ordinate: reflected intensity). So-S6 are different modes of operating the FLIPPER monochromator.

Fig. 3 Geometry of the alignment errors due to a displacement of a point source S parallel and perpendicular to the axis of an ideal ellipsoid. For other parameters see text.

Fig. 4 Intensity distributions calculated as a function of ΔI_{ax} at constant values of Δs_{lat} = 0.4 mm and ϕ = 45° (see Fig. 3)

Fig. 5a Calculated radial intensity distribution (PSF) in the focal plane with meridional (Θ_m) and sagittal (Θ_s) mean square surface errors, diffraciton is neglected, the radius is given in units of (Θ_m).

5b Contrast (MTF) calculated as a function of the spatial frequency $1/\lambda_x$ for different values of the mean square errors of the mirror.

Fig. 6a Calculated Fraunhofer diffraction pattern for the actual mirror parameters. The inserted frame is an extension of the left side in a linear scale. λ_{ph} denotes the photon wavelength.

Fig. 6b Integrated intensities of diffraction patterns of the type shown in Fig. 6a for different values of e. The integration is carried out over diaphragms with diameters 2 • "Radius/λ_{ph}".

Fig. 6c Calculated contrast (MTF) based exclusively on the diffraction features, neglecting geometrical errors of imaging for different types of coherence (see text).

Fig. 7 Schematic diagram of the microscope (not true to scale), $h\nu$ marks the direction of incoming synchrotron light.

Fig. 8 One dimensional scanning stage.

Fig. 9 Schematic diagram of the experimental chamber.

Fig. 10 Line-scan through focus illuminated by 2 eV photons from a HeNe-Laser.

Fig. 11 Line-scan through focus illuminated by 21.2 eV photons from a He discharge lamp using a 3 μm diameter entrance aperture. The distribution has a FWHM of less than 0.35 μm.

Fig. 12 Long-range line-scan through focus using the HeI line using a 100 μm entrance aperture.

Fig. 13 Long-range line-scan through focus using synchrotron radiation of 1100 eV photon energy.

Fig. 14 Two dimensional scan of the focus shown in Fig. 11. The frame is 2.26 x 2.48 μm², $h\nu$ = 21.2 eV.

Fig. 15 Transmission of a fine Cu grid, partly obstructed by two coarser supporting grids. The frame is 140 x 150 μm², $h\nu$ = 260 eV

Fig. 16 Total electron yield of an unsupported Fresnel zone plate made of gold. The frames and photon energies are
a) 140 x 150 μm², $h\nu$ = 400 eV,
b) 3.6 x 3.9 μm², $h\nu$ = 700 eV,

Fig. 17 Experimental MTF. The points are obtained from pictures taken at different radial regions of the zone plate, the curve is an interpolation.

Fig. 18 Energy distribution curve (EDC) of photoelectrons emitted from a 10 μm diameter gold spot on silicon, $h\nu$ = 330 eV.

Fig. 19 EDC of copper, $h\nu$ = 120 eV.

Fig. 20 Line scan of copper mesh, $h\nu$ = 120 eV,
bottom curve: transmission, top curve: Cu3d intensity.

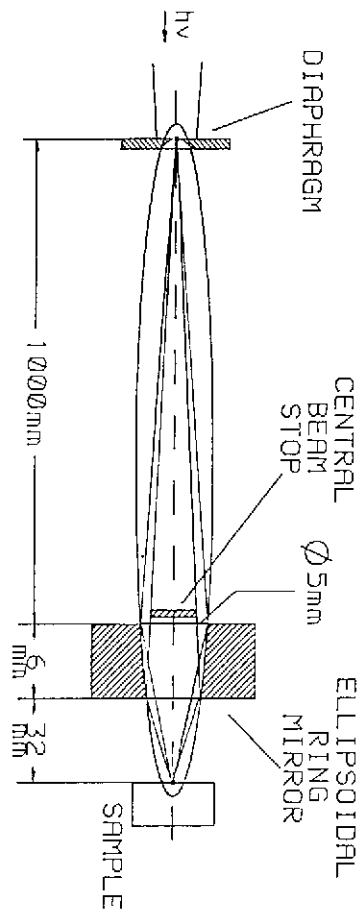

Fig.1

Fig.3

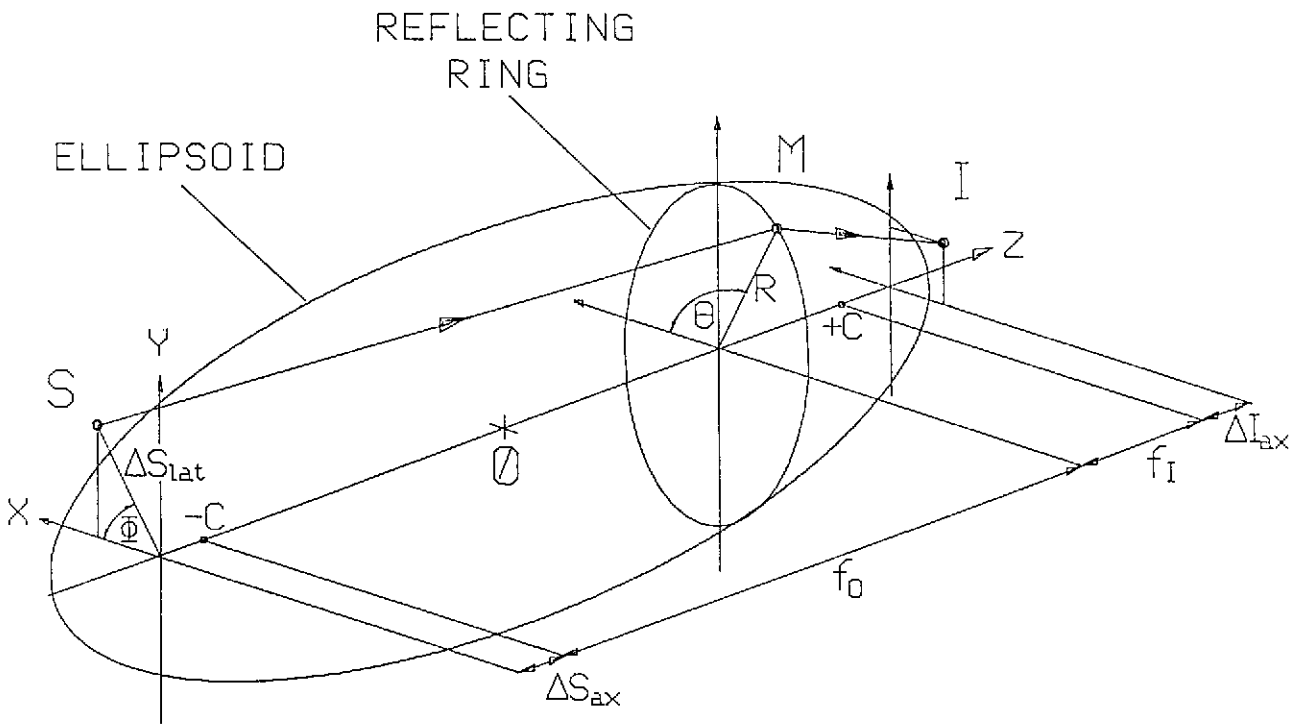
REFLECTING
RING
ELLIPSOID
M
I
Z
R
θ
+C
S
Y
X
ΔS_lat
Φ
-C
f_I
ΔI_ax
f_0
ΔS_ax

Fig.2

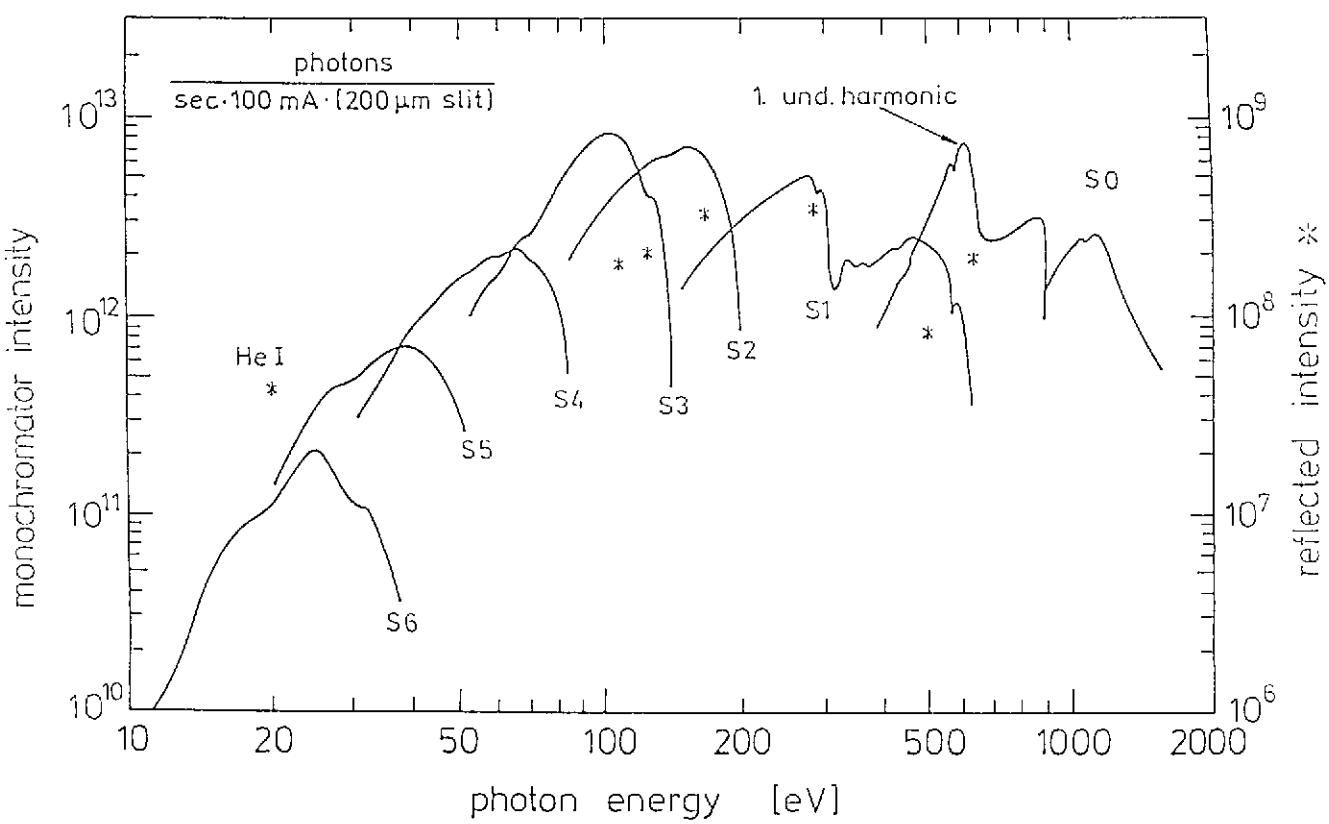
photons
sec·100 mA·(200 μm slit)
1. und. harmonic
He I
S0
S1
S2
S3
S4
S5
S6
monochromator intensity
reflected intensity *
photon energy [eV]
10^13
10^12
10^11
10^10
10^9
10^8
10^7
10^6
10
20
50
100
200
500
1000
2000

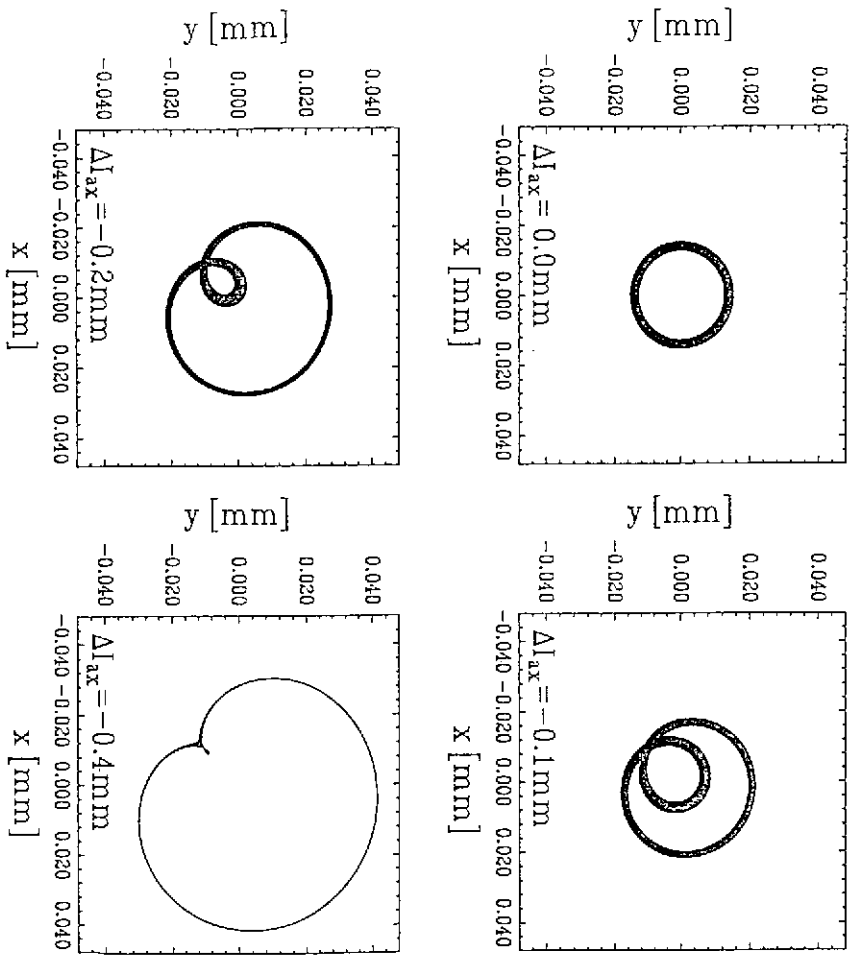
y [mm]
x [mm]
ΔI_{ax}= 0.0mm
ΔI_{ax}=−0.2mm
ΔI_{ax}=−0.1mm
ΔI_{ax}=−0.4mm
−0.040
−0.020
0.000
0.020
0.040

Fig.4

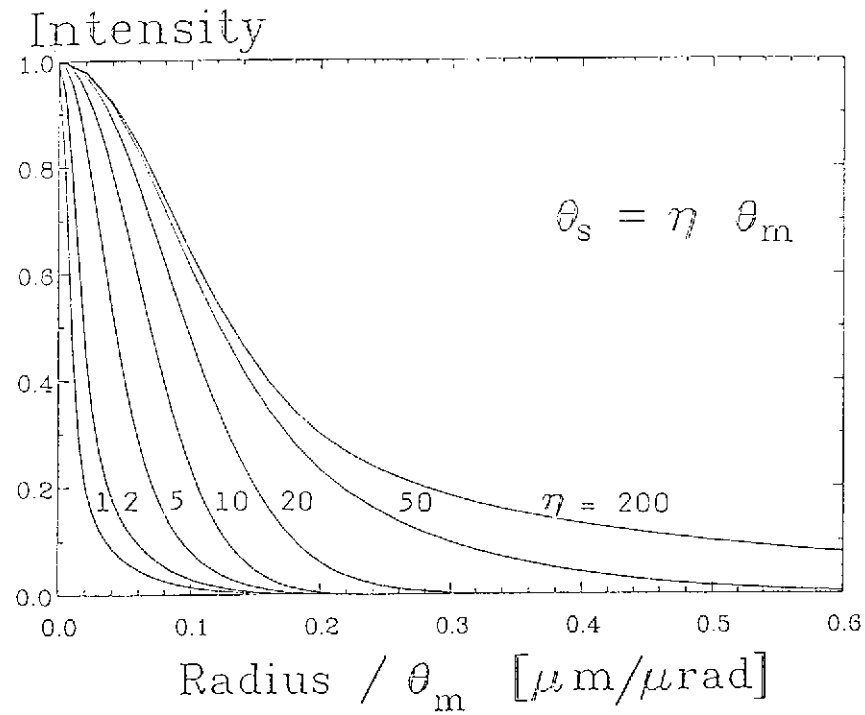
Intensity
$\theta_s = \eta \ \theta_m$
1
2
5
10
20
50
η = 200
0.0
0.2
0.4
0.6
0.8
1.0
0.1
0.3
0.5
Radius / θ_m [μm/μrad]

Fig.5a

Fig.6

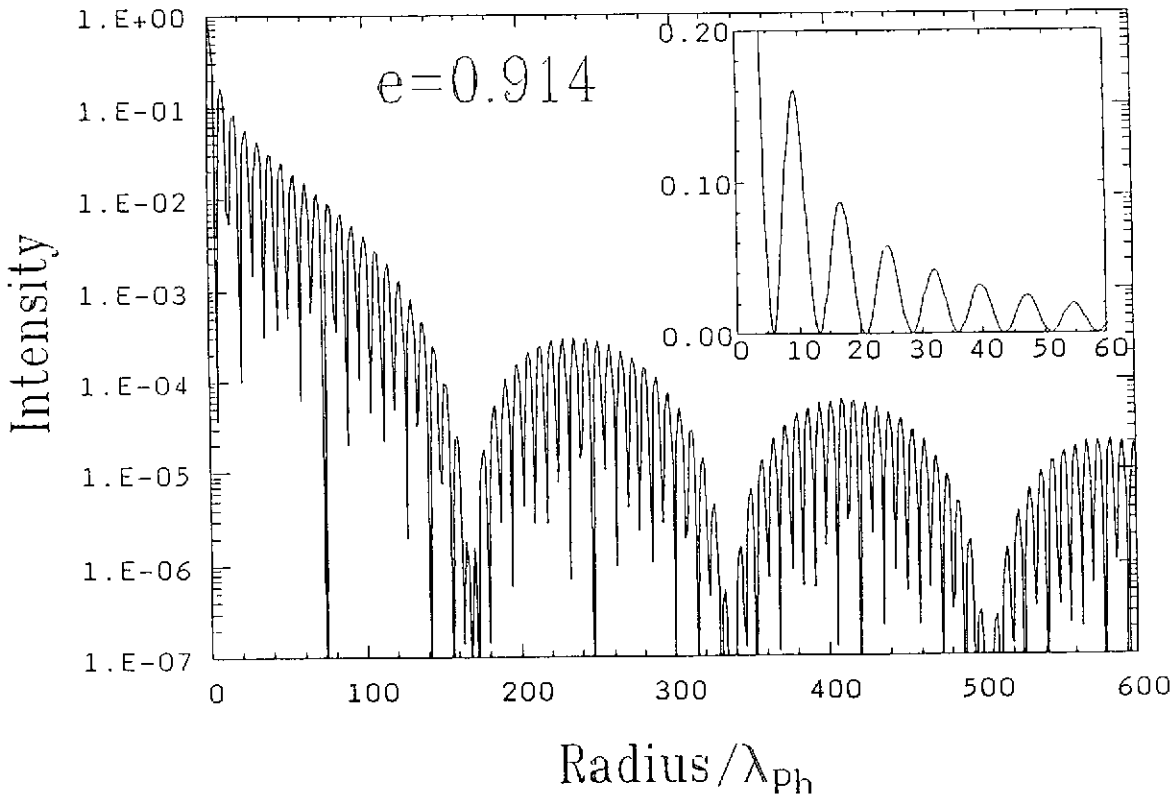
Fraunhofer Diffraction
e=0.914
Intensity
Radius/λph
1.E+00
1.E-01
1.E-02
1.E-03
1.E-04
1.E-05
1.E-06
1.E-07
0
100
200
300
400
500
600
0.20
0.10
0.00
0
10
20
30
40
50
60

Fig.5b

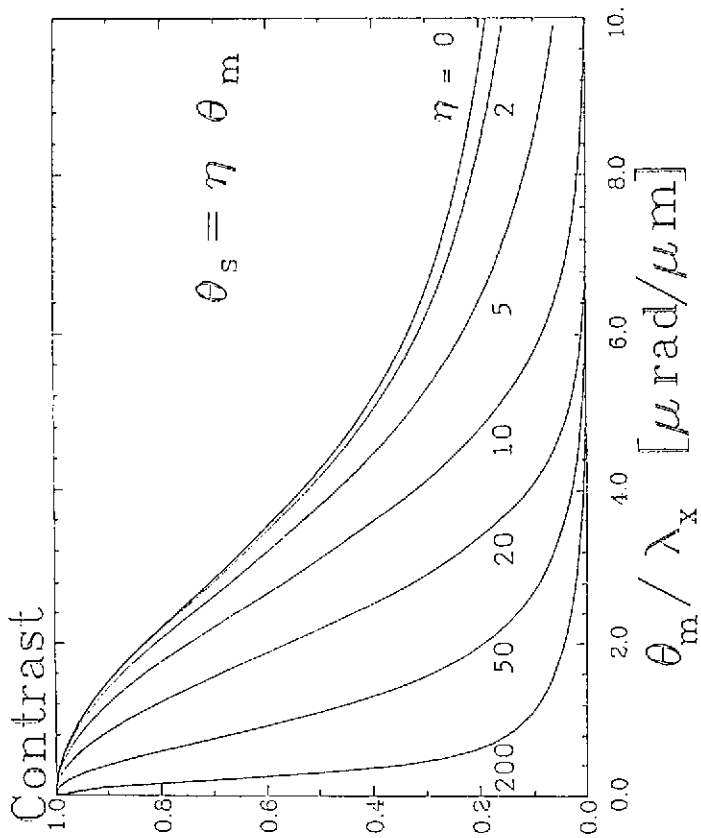
Contrast
θs = η θm
η = 0
2
5
10
20
50
200
1.0
0.8
0.6
0.4
0.2
0.0
0.0
2.0
4.0
6.0
8.0
10.
θm / λx [μrad/μm]

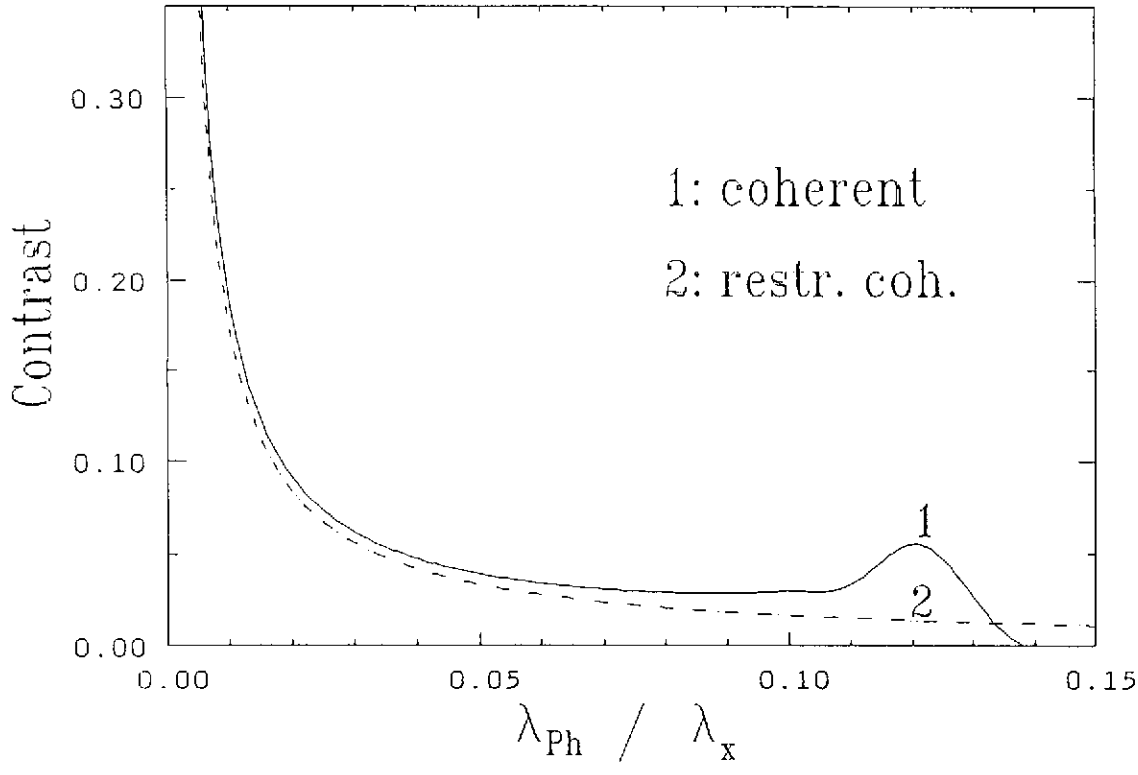
Contrast
0.30
0.20
0.10
0.00
1: coherent
2: restr. coh.
1
2
0.00
0.05
0.10
0.15
λPh / λx

Fig.6c

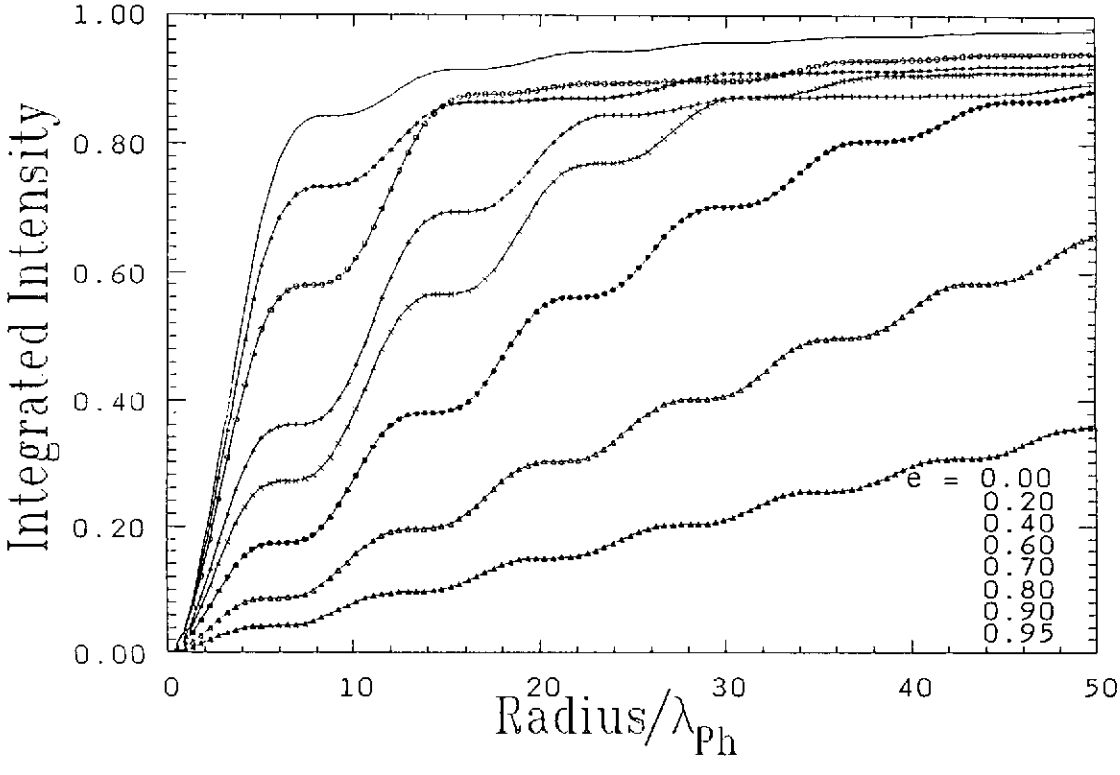
Integrated Intensity
1.00
0.80
0.60
0.40
0.20
0.00
e = 0.00
0.20
0.40
0.60
0.70
0.80
0.90
0.95
0
10
20
30
40
50
Radius/λPh

Fig.6b

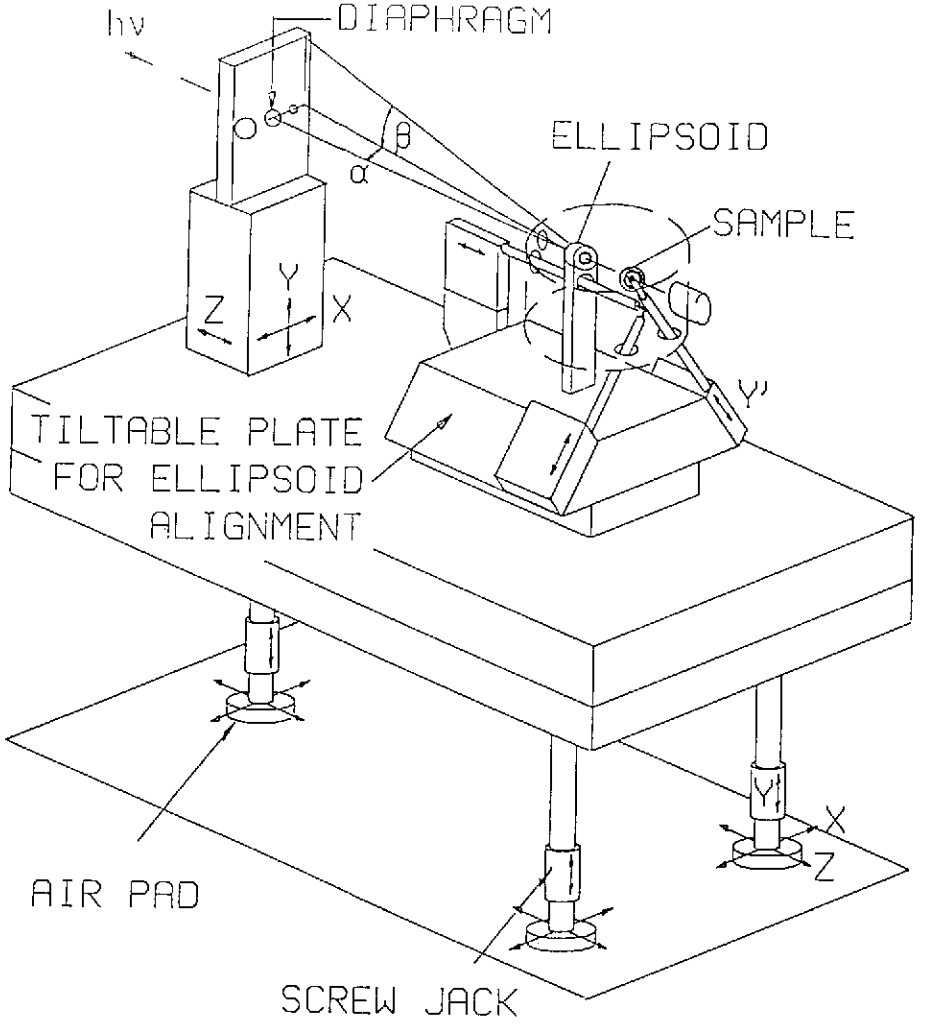
hν
DIAPHRAGM
ELLIPSOID
SAMPLE
β
α
Z
Y
X
Y'
TILTABLE PLATE
FOR ELLIPSOID
ALIGNMENT
AIR PAD
SCREW JACK
Y
X
Z

Fig.7

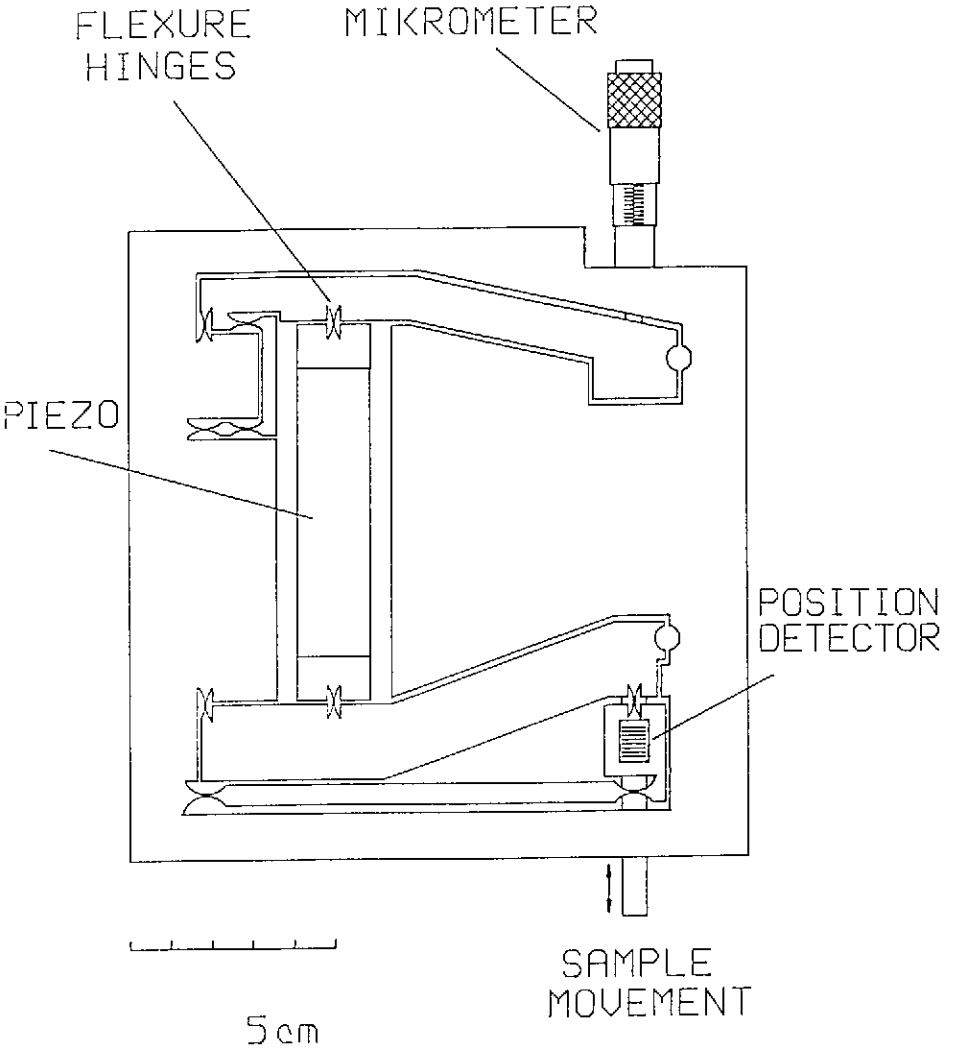
FLEXURE
HINGES
MIKROMETER
PIEZO
POSITION
DETECTOR
SAMPLE
MOVEMENT
5cm

Fig.8

Fig.10

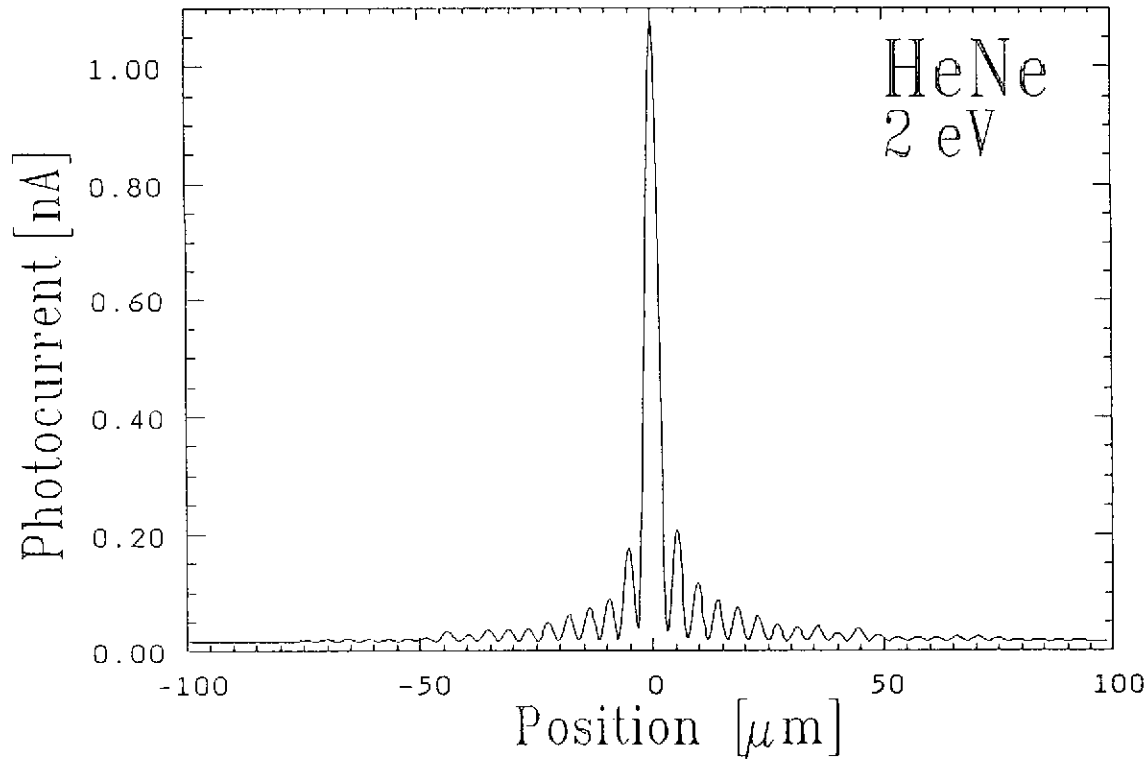
HeNe
2 eV
Photocurrent [nA]
1.00
0.80
0.60
0.40
0.20
0.00
-100
-50
0
50
100
Position [μm]

Fig.9

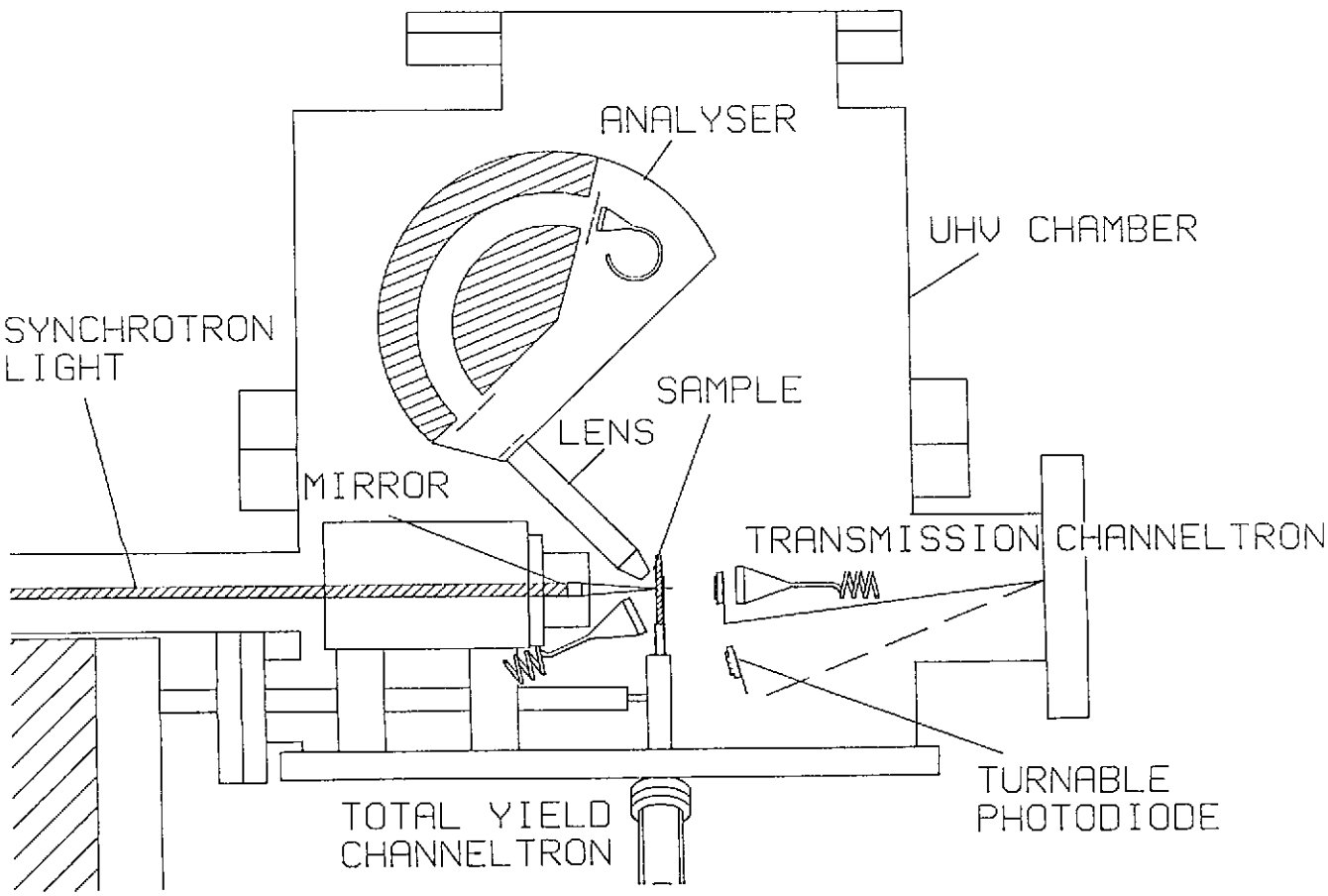
ANALYSER
UHV CHAMBER
SYNCHROTRON
LIGHT
SAMPLE
LENS
MIRROR
TRANSMISSION CHANNELTRON
TURNABLE
PHOTODIODE
TOTAL YIELD
CHANNELTRON

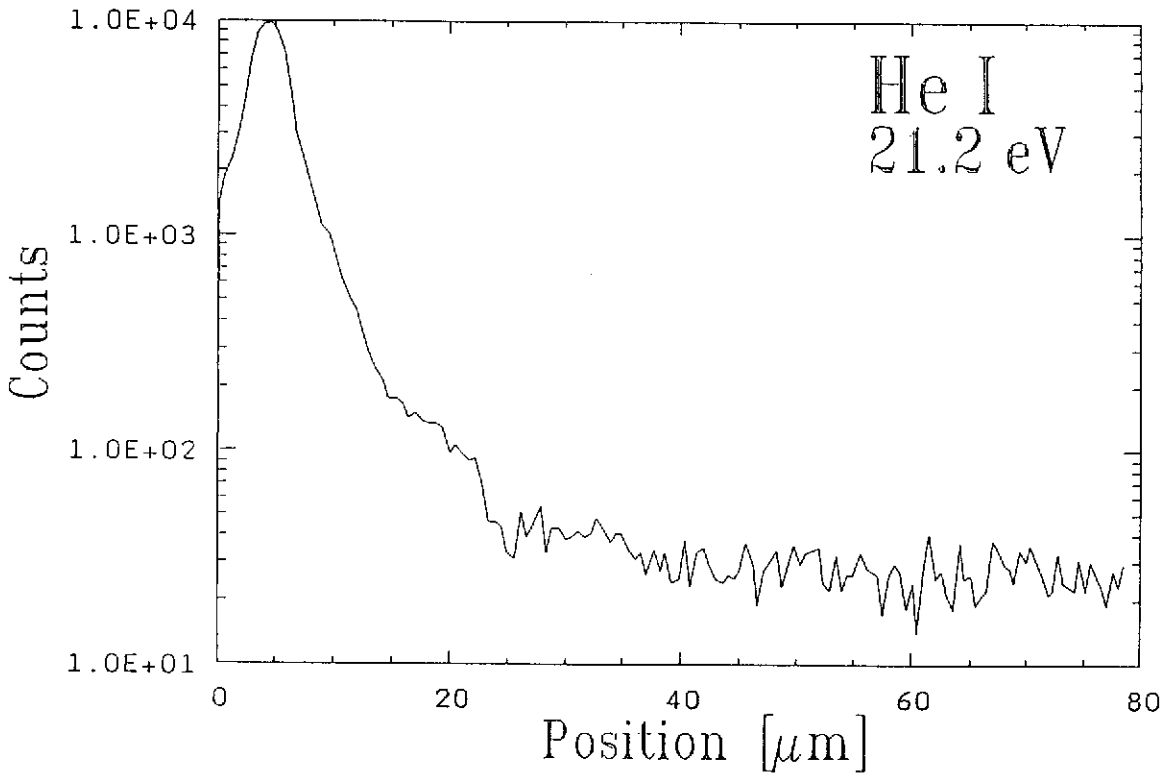
1.0E+04
1.0E+03
1.0E+02
1.0E+01
Counts
He I
21.2 eV
0
20
40
60
80
Position [μm]

Fig.12

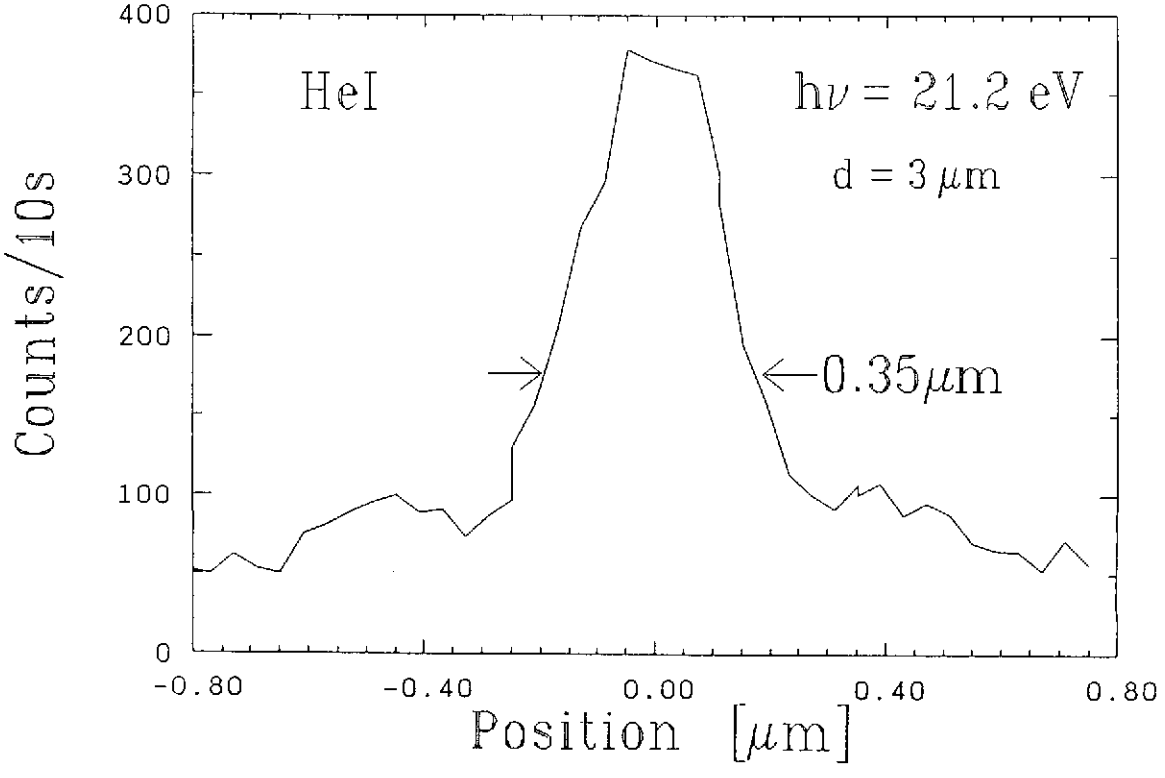
400
300
200
100
0
Counts/10s
HeI
hν = 21.2 eV
d = 3 μm
0.35μm
-0.80
-0.40
0.00
0.40
0.80
Position [μm]

Fig.11

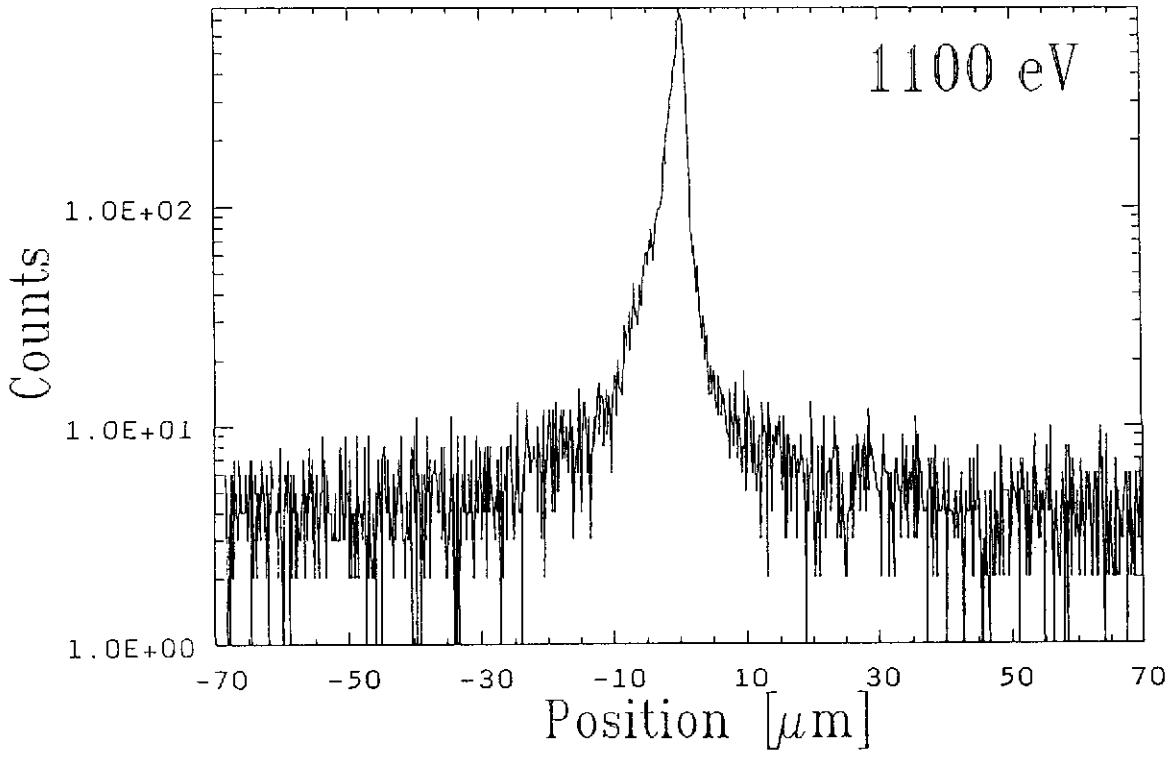
1100 eV
Counts
1.0E+02
1.0E+01
1.0E+00
-70
-50
-30
-10
10
30
50
70
Position [μm]

Fig.13

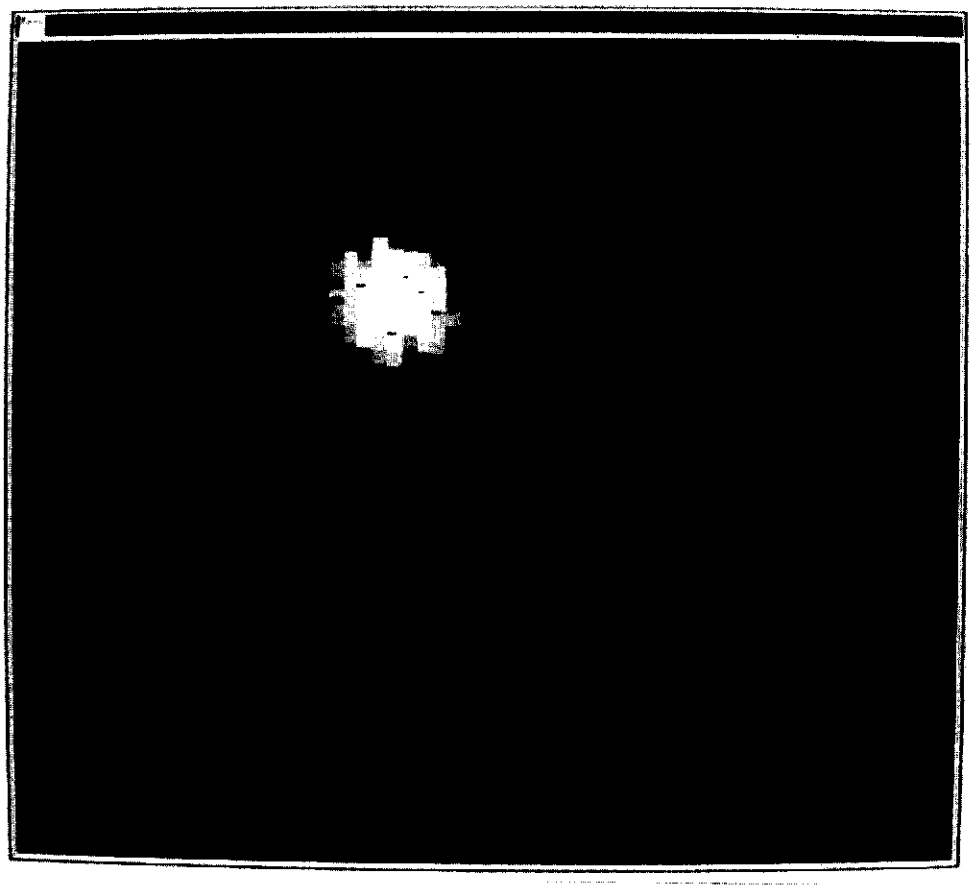

Fig.14

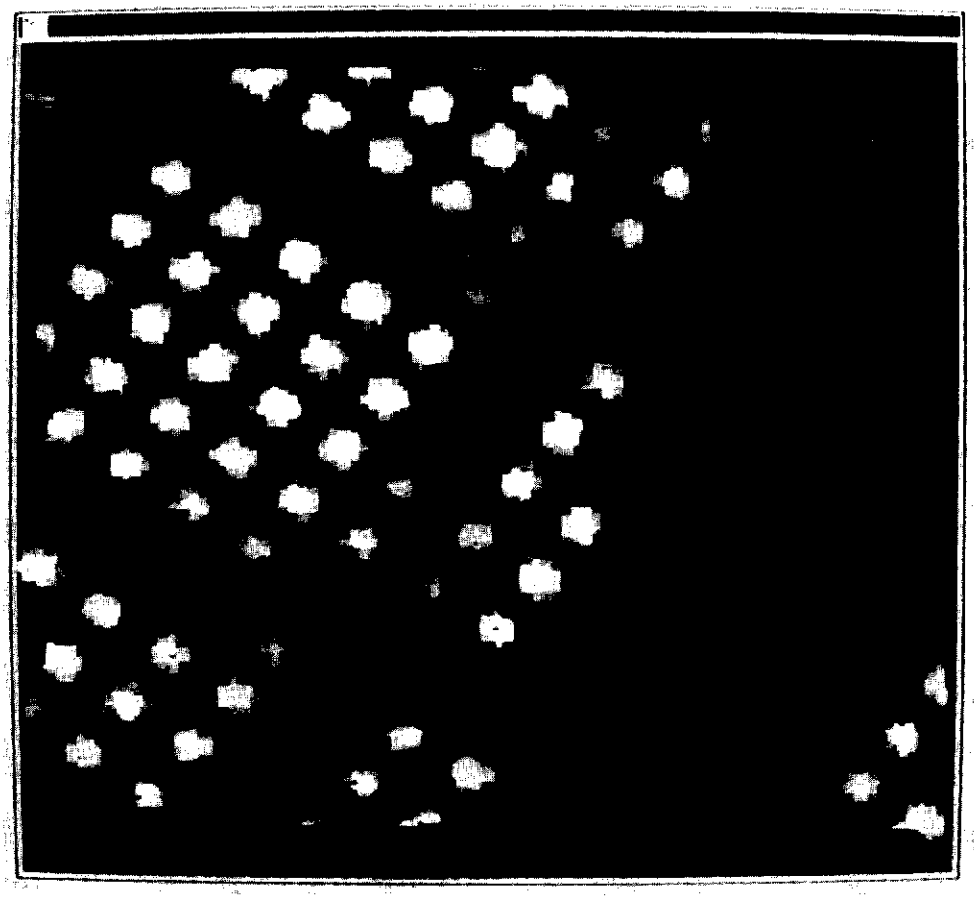

Fig.15

Fig. 16a

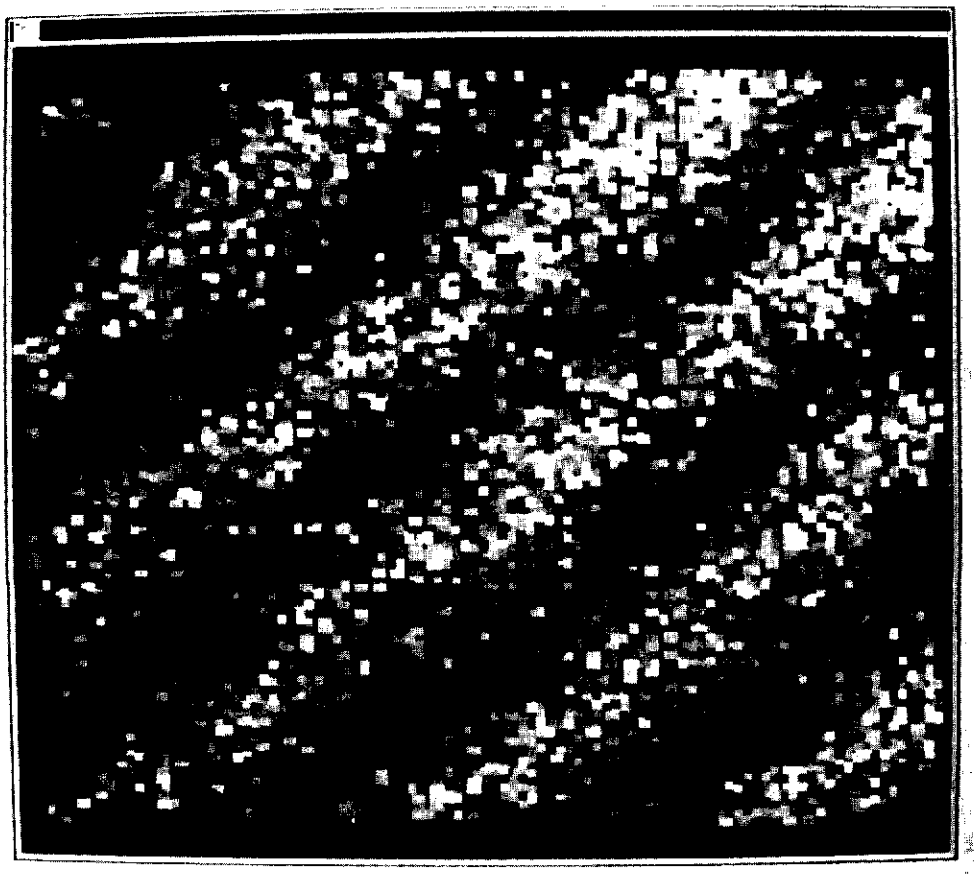

Fig. 16b

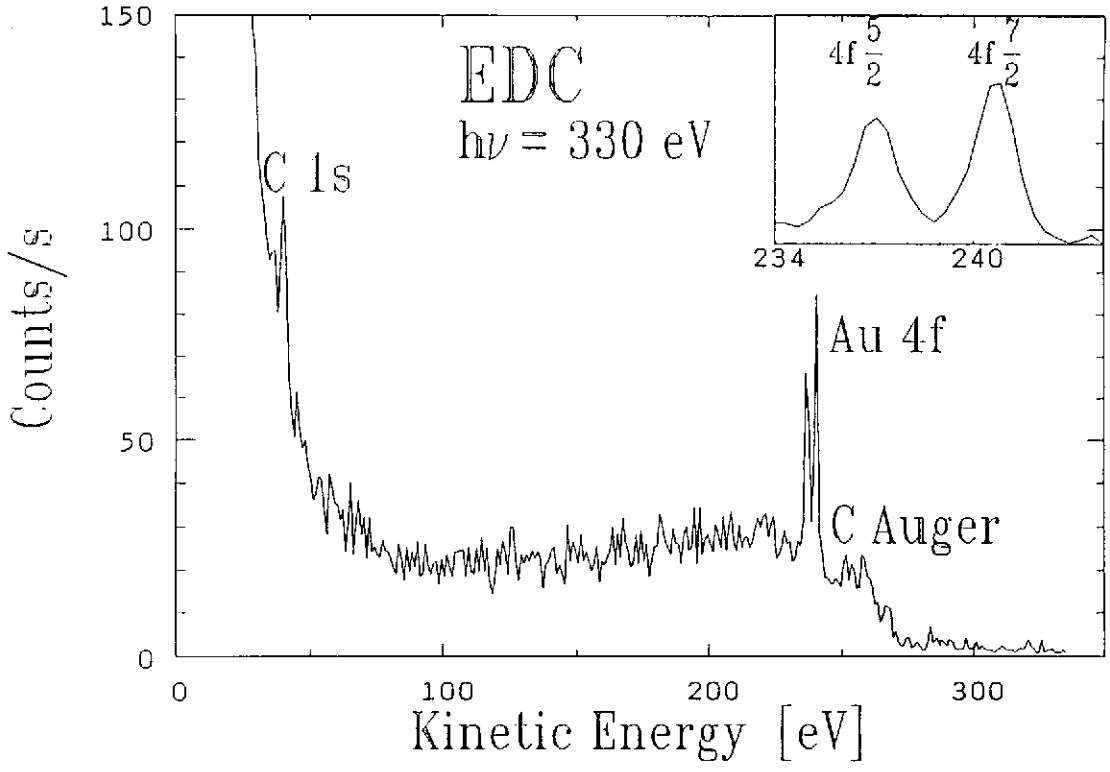
EDC
hν = 330 eV
C 1s
Au 4f
C Auger
4f 5/2
4f 7/2
234
240
Counts/s
Kinetic Energy [eV]
0
50
100
150
0
100
200
300

Fig.18

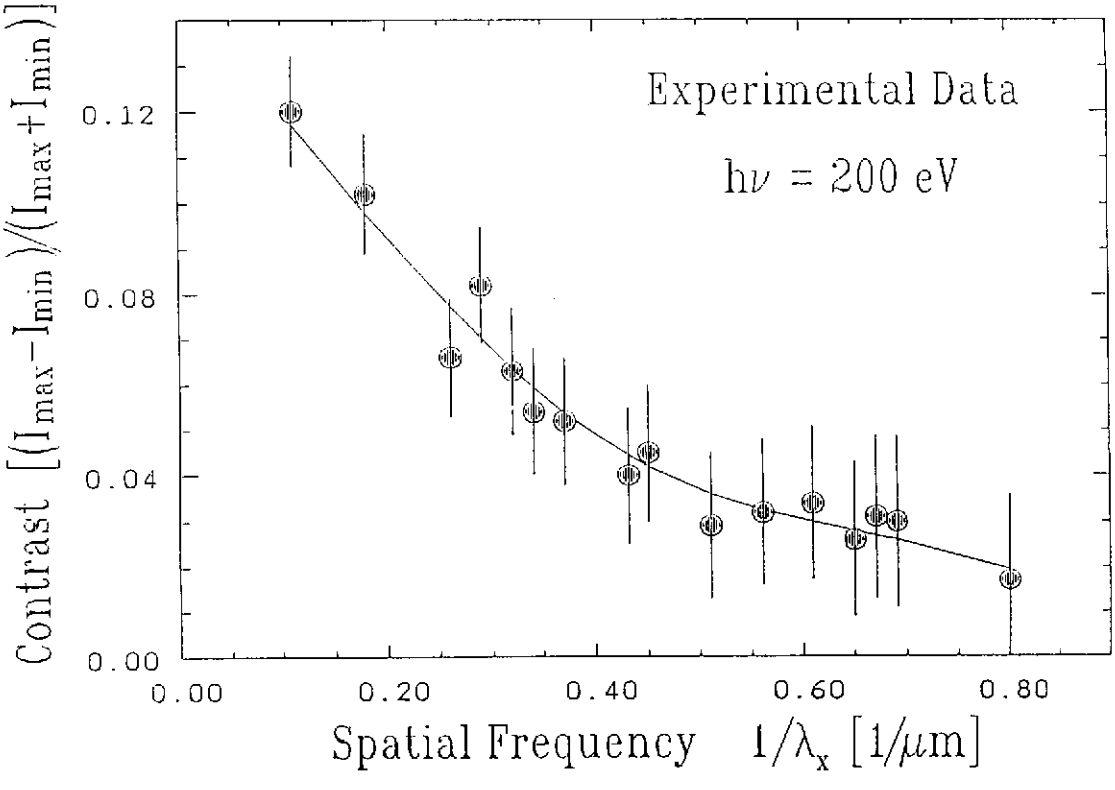
Experimental Data
hν = 200 eV
Contrast [(Imax−Imin)/(Imax+Imin)]
Spatial Frequency 1/λx [1/μm]
0.00
0.04
0.08
0.12
0.00
0.20
0.40
0.60
0.80

Fig.17

Fig.20

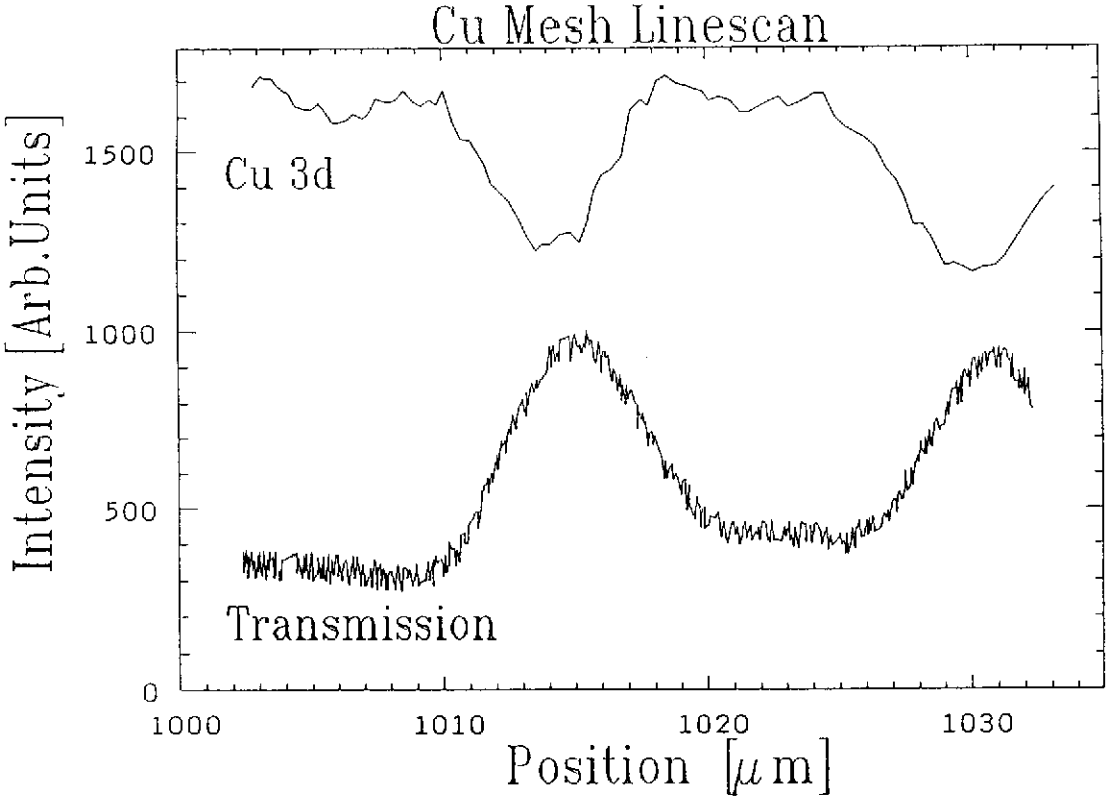
Cu Mesh Linescan
Intensity [Arb.Units]
1500
1000
500
0
Cu 3d
Transmission
1000
1010
1020
1030
Position [μm]

Fig.19

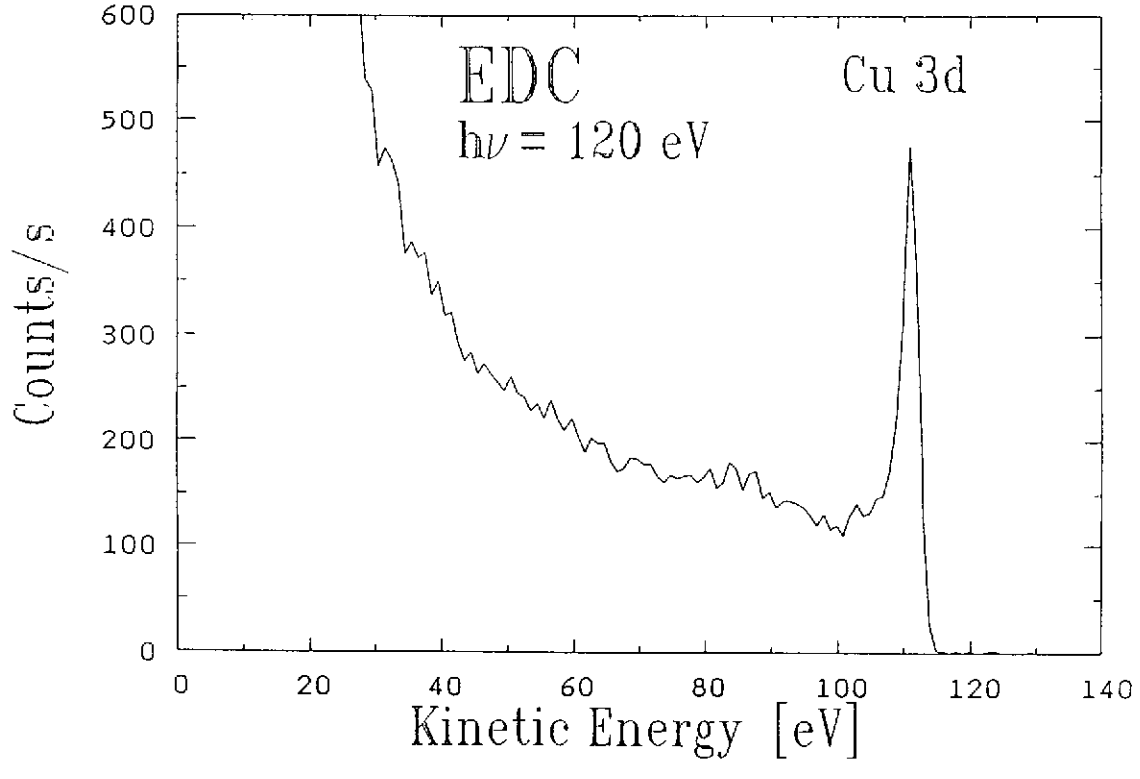
EDC
hν = 120 eV
Cu 3d
Counts/s
600
500
400
300
200
100
0
0
20
40
60
80
100
120
140
Kinetic Energy [eV]